Evaluation of biogenic zinc oxide nanoparticles from *Sonneratia ovata* leaf extract for multivariate factorial photocatalytic and biological activities

Kalidasan K [a,*], Chavanich S [a,b,**], Jagan K.S.G. [c], Surendhiran S [c], Naren Vidaarth T.M. [c], Karthik S [d], Kathiresan K [e], Jean Wan Hong Yong [f,g,***] [ORCID], Viyakarn V [a,b]

[a] *Center of Excellence for Marine Biotechnology, and Reef Biology Research Group, Department of Marine Science, Faculty of Science, Chulalongkorn University, Bangkok, Thailand*
[b] *Aquatic Resources Research Institute, Chulalongkorn University, Bangkok, Thailand*
[c] *Centre for Nanoscience and Technology, K.S. Rangasamy College of Technology, Namakkal (Dt.), Tiruchengode, Tamil Nadu, 637 215, India*
[d] *Laboratory of Cyanobacterial Biotechnology, Department of Biochemistry, Faculty of Science, Chulalongkorn University, Bangkok, 10330, Thailand*
[e] *Centre of Advanced Study in Marine Biology (CAS), Faculty of Marine Sciences, Annamalai University, Parangipettai, Tamil Nadu, India*
[f] *Department of Biosystems and Technology, Swedish University of Agricultural Sciences, Alnarp, 234 56, Sweden*
[g] *Future of Farming Institute, Faculty of Science and Engineering, Maastricht University, Venlo, 5928, The Netherlands*

ARTICLE INFO

ABSTRACT

The presence of dyes from industrial effluents (such as textile, paper, and leather industries) in water bodies is a significant source of pollution, posing ecological risks that necessitate their removal. The present study demonstrated that the mangrove *Sonneratia ovata* leaf extract is a promising resource for the biosynthesis of zinc oxide nanoparticles (ZnO NPs), which have potential applications in biomedical fields and wastewater remediation. X-ray diffraction analysis revealed that these nanoparticles have a hexagonal wurtzite structure. Optical measurements indicated the presence of a band gap at 3.19 eV. Morphological studies indicated a mixture of rod-shaped and small spherical nanoparticles. The observed physicochemical properties of the green-synthesized ZnO NPs significantly surpassed the chemically prepared ZnO NPs following a similar synthesis approach. The photocatalytic efficiency of the biosynthesized nanoparticles was tested under UV light irradiation to degrade ethidium bromide dye. This degradation efficiency was shown to be dependent on dye concentration, dye pH, and catalyst concentration. The highest degradation rates of 88.5 %, 98.6 %, and 89.4 % for ethidium bromide dye, respectively, are for dye concentration, dye pH, and nanocatalyst concentration following a first-order kinetic model. Furthermore, the stabilized nanoparticles derived from the green synthesis using *S. ovata* leaves are potent antioxidants, exhibiting antibacterial activity against *Staphylococcus aureus* and *Escherichia coli*. These findings highlighted the potential of using natural aqueous extracts from

S. ovata to produce phytochemical-enhanced nanoparticles with significant photocatalytic degradation of toxic dyes in water bodies and biomedical applications.

1. Introduction

Ethidium bromide (EtBr) is a well-known intercalating agent used extensively in molecular biology laboratories, primarily for staining nucleic acids in gel electrophoresis. It is an aromatic heterocyclic compound with the chemical formula $C_{21}H_{20}BrN_3$, and its structure consists of a tricyclic phenanthridine ring system (Nafisi et al., 2007; Tsuboi et al., 2007). The compound is positively charged due to a quaternary ammonium group, which facilitates its interaction with the negatively charged DNA and RNA molecules (Li et al., 2020). EtBr functions by intercalating between the base pairs of double-stranded DNA. Furthermore, this intercalation process involves the insertion of the planar phenanthridine ring between the stacked bases of the DNA helix. The interaction results in a distortion of the DNA structure, accompanied by an increase in the fluorescence of EtBr. EtBr exhibits a characteristic orange fluorescence under UV light when bound to DNA, making it a powerful tool for visualizing nucleic acids in agarose and polyacrylamide gels. Despite its widespread use, EtBr poses significant safety and environmental concerns due to its mutagenic and toxic properties (Reema et al., 2024; Song et al., 2020). The improper disposal of EtBr waste usually occurs from several point sources such as laboratories and certain industries using EtBr; leading to the leaching of the contaminants into adjacent water bodies and soil. The discharge of EtBr into the ecosystem has been reported to cause significant environmental issues, including water pollution, eutrophication, and disruption of aquatic life. As an intercalating agent, EtBr can cause mutations by inserting itself into the DNA of living organisms, leading to potential carcinogenic effects (Johnson et al., 2003; Abdel-Salam et al., 2012). Several abnormalities have been reported and arising from the exposure to EtBr in various organisms. Vacquir et al. have reported the chromosomal abnormalities found in sea urchin eggs when exposed to EtBr, which resulted in abnormal division of cells (Vacquier and Brachet, 1969). Similarly, Naum et al. have identified that the EtBr can induce respiratory mutations in cultured human cells by limiting the activity of the mitochondrial enzyme cytochrome oxidase (Naum and Pious, 1971). Von Wurmb-Schwark et al. have witnessed a mitochondrial DNA breakdown that occurred with the usage of EtBr, which decreased the mitochondrial DNA content, resulting in cell death (von Wurmb-Schwark et al., 2006). Ouchi et al. have studied EtBr causes genotoxic effects in *Drosophila melanogaster* even at the lower concentration, which significantly affects the productivity and morphology of the species (Ouchi et al., 2007).

Given EtBr's environmental and health risks, its removal from water bodies and contaminated environments is a subject of considerable interest. Photocatalytic degradation has emerged as a promising approach for removing organic pollutants such as EtBr, offering several distinct advantages over traditional chemical and physical methods (Swetha and Balakrishna, 2011; Lavand and Malghe, 2016; Biswal et al., 2021; Adán et al., 2007). One of the primary benefits is its environmental friendliness. Photocatalytic processes typically completely mineralize organic contaminants into harmless byproducts such as carbon dioxide and water, unlike traditional methods that may produce toxic intermediates. Moreover, photocatalysis operates under mild conditions, such as room temperature and atmospheric pressure, which reduces energy consumption and minimizes the overall environmental footprint. Several semiconductive photocatalyst nanomaterials have been employed to degrade distinct organic pollutants such as TiO_2 (titanium dioxide), ZnO (Zinc oxide), NiO (Nickel oxide), SnO_2 (Tin oxide), Co_3O_4 (Cobalt oxide), Fe_2O_3 (Iron oxide) and CdS (Cadmium sulfide) (Hitam and Jalil, 2020; Sun et al., 2022; Almenia et al., 2023; Devabharathi et al., 2024; Peiris et al., 2021; Kandasamy et al., 2023). Notably, photocatalysts like ZnO NPs exhibit strong oxidative power when sufficient light is available, leading to high degradation efficiency. This process thoroughly removes pollutants by breaking them down entirely into inorganic substances; compared to the other partial degradation or separation methods that may leave residual contaminants.

The synthesis of ZnO NPs via green chemistry approaches has gained considerable attention as a sustainable and eco-friendly alternative to conventional synthesis methods (Bandeira et al., 2020; Doan Thi et al., 2020; Hanif et al., 2024). Green synthesis methods utilize biological materials, such as plant extracts, microorganisms, and other natural resources, to reduce the metal ions and stabilize the resulting nanoparticles (Subramani et al., 2025). These methods align with the principles of green chemistry, aiming to minimize the use of hazardous substances, reduce energy consumption, and generate less waste. *Sonneratia ovata*, commonly known as mangrove apple, is a species of mangrove plants found in coastal and estuarine environments in Southeast Asia and other tropical regions (Saenger et al., 2019). It belongs to Lythraceae and is characterized by its ability to thrive in saline and waterlogged conditions. This unique eco-physiological resilience of *Sonneratia* makes it an important ecological component within the mangroves, providing habitats for many organisms and protection against coastal erosion (Zimmer et al., 2022). Interestingly, *S. ovata* is rich in diverse bioactive compounds, making it a valuable resource for green chemistry applications (Liu et al., 2023).

The phytochemical composition of *S. ovata* includes polyphenols, proteins, amino acids, polysaccharides, vitamins, minerals, saponins, and terpenoids (Liu et al., 2023; Puspitasari et al., 2022). These compounds play critical roles in reducing and stabilizing metal ions during nanoparticle synthesis. Polyphenols, such as flavonoids and tannins, possess potent antioxidant properties and are instrumental in lowering zinc ions (Zn^{2+}) to ZnO NPs. Proteins and amino acids serve as reducing agents and stabilizers, facilitating the formation of nanoparticles by preventing agglomeration through capping. Polysaccharides, including cellulose, hemicellulose, and pectin, provide a stabilizing matrix to support nanoparticle formation and molecular stability (Astuti et al., 2023; Nguyen et al., 2024).

Numerous studies have explored the photocatalytic degradation of EtBr under UV irradiation; however, the development of green-synthesized photocatalysts capable of delivering efficient EtBr degradation remains limited. In the present work, we described a novel photocatalytic approach using the preparation of controlled morphology ZnO NPs by employing *S. ovata* (a mangrove species) as a reducing and stabilizing agent. The synthesized nanoparticles are then characterized using various techniques to assess their properties

comprehensively. X-ray diffraction (XRD) is employed to determine their crystallographic structure, while the Field emission scanning electron microscopy (FESEM) is used to analyze their morphological features. Additionally, thermal gravimetric analysis (TGA) provides insights into their thermal stability, and Fourier-transform infrared spectroscopy (FTIR) identifies the functional groups present. The specific surface area of the NPs is evaluated using the Brunauer-Emmett-Teller (BET) analysis, and the UV–visible spectroscopy was harnessed to assesses their optical properties. These detailed characterizations help us to understand the properties and potential applicationsof the green-synthesized ZnO NPs.

2. Experimental procedure

2.1. Materials and methods

ZnO NPs synthesis was conducted using high-purity reagents and materials to ensure accurate and reliable results. Zinc acetate (Zn $(CH_3COO)_2$) (99 % purity) was used as the zinc source for the synthesis of ZnO NPs. Sodium hydroxide (NaOH) (99 % purity) was used chemical reducing agent for the chemical method. It was purchased from Loba Chemie, India. Fresh *Sonneratia ovata* leaves were collected from Same Sarn Islands, Upper Gulf of Thailand, thoroughly washed, and used to prepare the extracts for the green synthesis process. The synthesis and washing processes used ethanol (99.9 % purity) and double-distilled water. The voucher specimen of *S. ovata* (specimen number: A 17869) has been deposited at the Chulalongkorn University Herbarium (herbarium code: BCU), Thailand, and serves as the official reference for species identification.

2.2. Preparation of S. ovata leaf extract

The leaves of *S. ovata* were collected and thoroughly washed multiple times with double-distilled water to remove any surface contaminants and impurities. After washing, the leaves were shade-dried for 36 h to ensure complete moisture removal. Once dried, the leaves were finely ground using a domestic blender to achieve a homogeneous powder. A total of 10 g of the powdered leaves were then dispersed in 100 mL of preheated double-distilled water at 60 °C. The mixture was stirred for 6 h using a magnetic stirrer to facilitate the extraction of bioactive compounds. After extraction, the mixture was centrifuged at 3000 rpm for 20 min to separate the solid residue from the liquid extract. The resulting supernatant containing the bioactive compounds was collected and utilized to synthesize ZnO NPs; the phytochemicals might help reduce the precursor's metal ions and eventually stabilize the particles.

2.3. Synthesis of ZnO nanoparticles: green and chemical method

To produce ZnO NPs through a green synthesis approach, initially, 100 mL of *S. ovata* extract was heated to 70 °C. A 0.1 M zinc acetate (1.834 g) solution was added to this extract, and the mixture was continuously stirred for 3 h. Subsequently, the solution underwent an ultrasonic probe sonication process for 120 min at a frequency of 40 kHz, with the sonication parameters set to 8 s of working time followed by a 5-s break. After sonication, the solution was allowed to stand at room temperature for 24 h to facilitate homogeneous nucleation and growth of the nanoparticles. Following incubation, the solution was centrifuged at 6000 rpm for 15 min. The resulting pellet was washed multiple times with 40 % ethanol and double-distilled water to remove residual impurities. The
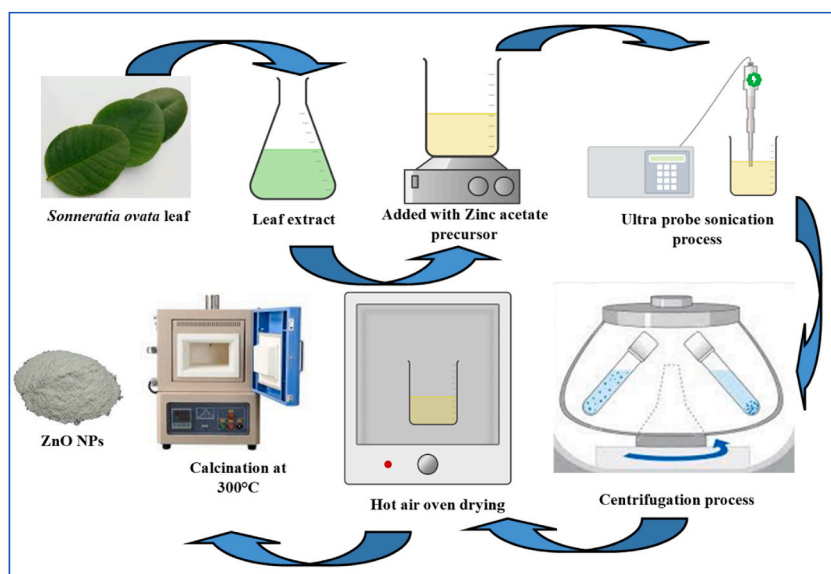

Fig. 1. Schematic representation of the ZnO NPs synthesis process using the mangrove *Sonneratia ovata*.

washed pellet was then dried in a hot-air oven at 60 °C for 7 h. Once dried, the pellet was finely ground and calcined at 300 °C in a muffle furnace. The resulting white powder was identified as ZnO-S. A brief schematic representation is provided in Fig. 1 for the whole synthesis process of ZnO NPs.

The ZnO NPs were produced similarly through a chemical method: 1 M NaOH was dissolved in 100 mL DD water under constant stirring. Then, 0.1 M of Zinc acetate solution of 100 mL was added slowly to the mixture and continuously stirred for 3 h at 70°. The solution was then subjected to sonication with as mentioned parameters followed by green synthesis preparation. The nucleation growth phase, drying, and calcination duration were followed as per the green synthesis procedure. The similarity of the following methods parallel with green synthesis methodology offers a direct comparison of the physicochemical properties of prepared samples. The chemical route prepared ZnO NPs were further referred to as ZnO-N.

2.4. Characterization techniques

The crystallographic properties of prepared ZnO NPs were evaluated using Powder X-ray Diffraction analysis (XRD) (X'pert pro; Netherlands). The study was conducted from the 2θ range 5°–80°, with a step size of 0.02. The morphological properties and chemical composition of the samples were analyzed using a Field emission scanning electron microscope (FESEM) (Carl Zeiss – Sigma 300, German). The functional group characteristics were evaluated using Fourier transform infrared spectroscopy (FTIR) (Spectrum 100, USA). Furthermore, the particle size of the prepared samples was assessed using a Particle size analyzer (PSA) (Nanophox; Germany) following the Dynamic light scattering technique with a scattering angle of 120°. The optical properties of prepared nanomaterials were evaluated using UV–Vis spectroscopy (UV–Vis) (Cary 8454; Agilent, Singapore). The measurements were taken between the wavelength 190–800 nm, and the band gap of the materials was calculated using the Tauc plot method. Further, the surface area and thermal properties of the prepared ZnO NPs were evaluated using BET (Brunauer Emmett Teller, AMI -Meso 112, USA) and Thermogravimetric analyzer (TGA) (Exstar TG/DTA 6300; Hitachi, Japan). The photocatalytic degradation of EtBr dyes was monitored using UV–Vis spectroscopy.

2.5. Antibacterial activity

2.5.1. Preparation of inoculum bacterial culture

The initial bacterial cultures for the antibacterial study, such as *Escherichia coli* (ATC9677) (*E. coli*) and *Staphylococcus aureus* (ATCCC6538P) (*S. aureus*), were purchased from the National Collection of Industrial Microorganisms (NCIM) at the National Chemical Laboratory in Pune, India. The loop of test bacteria was then introduced into the nutrient broth and incubated at 37 °C for 12 h for effective bacterial growth. The increased turbidity of the liquid indicates effective bacterial growth.

2.5.2. Muller Hinton agar method

The antibacterial properties of the synthesized ZnO NPs were assessed using the Mueller-Hinton agar plate method. For this evaluation, a microbial inoculum was evenly spread (500 μL) over the surface of Mueller-Hinton agar plates to create a uniform bacterial lawn. Wells were then carefully filled with different concentrations of ZnO NPs suspended in an appropriate solvent. The plates were incubated at 37 °C for 24 h for bacterial growth and interaction with the nanoparticles. A standard antimicrobial agent, streptomycin (25 mg/mL), was used as a control to benchmark the antibacterial activity of the ZnO NPs. After the incubation period, the inhibition zones around the wells containing ZnO NPs were measured. The diameter of these zones was used to evaluate and compare the antibacterial efficacy of the ZnO NPs against the standard antimicrobial agent.

2.6. Antioxidant activity

The antioxidant potential of the synthesized ZnO NPs was evaluated based on their ability to scavenge free radicals using the DPPH (2,2-diphenyl-1-picrylhydrazyl) assay. In this procedure, 100 mL of a 0.1 mM DPPH solution was prepared, and varying concentrations of ZnO nanoparticles (25, 50, and 100 mg/mL) were added. The mixture was incubated in the dark for 45 min to allow for the interaction between the nanoparticles and the DPPH radicals. Following incubation, the absorbance of the solution was measured at 517 nm using UV–Vis spectroscopy. The degree of free radical scavenging by the ZnO NPs was assessed based on the decrease in absorbance, which indicates the reduction of DPPH radicals. For comparison, the antioxidant activity of the ZnO NPs was also evaluated against *Sonneratia ovata* leaf extract, a natural antioxidant, to determine the relative effectiveness of the nanoparticles in scavenging free radicals. The free radical scavenging efficiency was estimated using the following formula:

$$\textit{Free radical scavenging activity } (\%) = \frac{A_c - A_t}{A_C} \times 100$$

Where A_c is the absorbance of the control (DPPH solution without nanoparticles), and A_t is the absorbance of the DPPH solution with ZnO nanoparticles.

2.7. Photocatalytic activity

The photocatalytic activity of the synthesized ZnO NPs was evaluated using EtBr as a model pollutant. Several operational pa-

rameters were systematically studied to optimize the degradation of EtBr. Initially, the photocatalytic performance of ZnO NPs at different concentrations (100, 200, 300, and 400 ppm) was determined with a fixed concentration of 10 ppm EtBr solution. Before irradiation, the catalyst was mixed with the EtBr solution in the dark and stirred for 30 min to ensure homogeneous adsorption equilibrium. Subsequently, the solution was subjected to UV irradiation using a UV chamber (Poshly T4-8 W) equipped with a magnetic stirrer for a fixed duration of 120 min. The absorbance of the EtBr solution was measured at 285 nm at 15-min intervals to monitor the degradation progress. In addition to optimizing the catalyst concentration, the effects of varying EtBr concentrations (20, 30, 40, and 50 ppm) and different pH levels (5, 9, 11, and 13) were also investigated. The methodology for these parameters was similar to that used for optimizing the catalyst concentration. The degradation efficiency was calculated using the following formula:

$$Degradation\ efficiency\ (\%) = \frac{C_0 - C_t}{C_0}$$

Where C_0 is the initial absorbance of the EtBr solution, and C_t is the absorbance after a given irradiation time. This formula quantifies the effectiveness of the ZnO NPs in degrading EtBr under various conditions.

2.8. Statistical analysis

The photocatalytic, antibacterial, and antioxidant activities were all performed in triplicate. The experimental data were statistically analyzed using Origin 8.5.1 software (OriginLab Corporation, USA), and the results are presented as mean $\pm$ SD.

3. Results and discussion

3.1. X-ray diffraction and refinement analysis

Fig. 2 depicts the powder XRD pattern of the synthesized ZnO-S and ZnO-N NPs, revealing their polycrystalline nature. The major diffraction peaks observed for ZnO-S are observed at 2θ positions of 31.7°, 34.3°, 36.2°, 47.5°, 56.5°, 62.8°, and 67.9°. Similarly, the peaks observed for ZnO-N NPs are 31.7°, 34.4°, 36.2°, 47.5°, 56.5°, 62.8°, and 67.9°. These peaks correspond to the crystal planes (010), (002), (011), (012), (110), (013), and (112), respectively, indicating a hexagonal wurtzite crystal structure with a P63mc space group, following JCPDS card no: 96-900-4182 (Mohammed and Abdul Karim, 2021; Torkamani et al., 2023). The average crystalline size of the prepared ZnO-S and ZnO-N NPs was calculated using the Debye-Scherrer formula (Nasiri et al., 2023)

$$D(crystallite\ size) = \frac{0.9\lambda}{\beta\ Cos\ \theta}$$

Where the wavelength of X-rays employed is represented as λ, the full-width half maximum of the peaks is denoted as β, 0.63, and θ represents the diffraction angle. The calculated average crystallite size of the ZnO-S and ZnO-N NPs is 24.6 nm and 35.42 nm, as shown in Table 1. The relatively smaller crystalline size observed in ZnO-S samples can be attributed to the faster nucleation and growth, producing a smaller crystalline size using *S. ovata* as a green reducing and stabilizing agent (Abuzeid et al., 2023). Additionally, the sonication approach employed during the synthesis promotes the formation of smaller, well-dispersed nanoparticles. This method enhances the nucleation process while limiting crystal growth, resulting in a reduced average crystallite size. Furthermore, the dislocation density (δ) of the prepared ZnO NPs was estimated using the following equation:

$$\delta = \frac{1}{D^2}$$

The dislocation density, presented in Table 1 for ZnO-S and ZnO-N NPs, was calculated to be 1.65×10^{-3} nm^{-2} and 0.797×10^{-3}
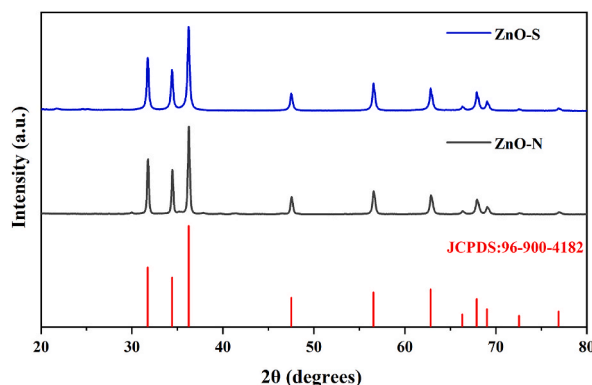

Fig. 2. a) X-ray diffraction graph obtained for prepared ZnO-S and ZnO-N NPs.

Table 1

The obtained XRD and Rietveld parameters of prepared ZnO nanoparticles.

Samples	Crystalline size (nm)	Dislocation Density ($\times 10^{-3}$ nm^{-2})	Lattice parameters	Rietveld fit parameters			
				R_p	R_{wp}	R_{exp}	Chi^2
ZnO-S	24.16	1.65	a = b = 3.253 Å, c = 5.207 Å	1.276	1.534	2.9	1.6
ZnO-N	35.42	0.797	a = b = 3.258 Å, c = 5.209 Å	1.688	1.923	2.54	1.79

nm^{-2}. The low dislocation density obtained for prepared ZnO-S NPs can be associated with high crystallinity and lower crystalline size. Furthermore, the XRD pattern, which does not possess any additional peaks, shows the absence of impurities in ZnO-S and ZnO-N NPs.

The Rietveld refinement analysis was conducted using FullProf analytical software to estimate the difference between the calculated and observed XRD patterns. This analysis optimized several operational parameters, including background, preferred orientation, and occupancies (Mandal et al., 2020; Arrasheed et al., 2021). The refinement process involved iterative parameter adjustments to best match the experimental data and the theoretical model. The obtained refinement parameters for the synthesized ZnO NPs are summarized in Table 1. The lattice parameters determined for the hexagonal crystal structure of ZnO-S are a = b = 3.253 Å and c = 5.207 Å. Similarly, the obtained lattice parameters for ZnO-N samples are a = b = 3.258 Å and c = 5.209 Å. These values are consistent with those reported in the literature for high-purity ZnO, confirming the successful synthesis of the desired crystalline phase (Nath et al., 2018; Zandi et al., 2011). The goodness of fit values (GoF) of the prepared ZnO NPs represent the optimal fit with the calculated data compared to previous findings. The GoF value is a vital indicator of the refinement quality and demonstrated an excellent match between the experimental and calculated XRD patterns. The reduced residual values and superior fit suggest that the refinement precisely depicts the crystal structure of the synthesized ZnO NPs. Moreover, the precise determination of lattice parameters and the goodness of fit values indicated that the green synthesis method using *S. ovata* as a reducing agent, coupled with the sonication approach, produces high-quality ZnO NPs with well-defined crystallographic properties. These results support the structural integrity of the synthesized nanoparticles and underscore the effectiveness of the environmentally friendly synthesis route.

3.2. Morphological and elemental composition analysis

The morphology of the synthesized ZnO NPs was examined using FESEM microscope. The FESEM images of ZnO-S sample, depicted in Fig. 3(a–b), reveal a predominance of spherical nanoparticles alongside partially formed hexagonal nano-rod structures. The high-resolution FESEM images indicate that these spherical nanoparticles are well-dispersed, with minimal agglomeration, suggesting effective stabilization by the green reducing agent, *S. ovata*. The bioactive compounds in the mangrove plant likely contribute to this stabilization, capping the nanoparticles and preventing excessive growth and aggregation. In addition to the spherical nanoparticles, the FESEM images also show hexagonal nano-rod structures. The formation of these hexagonal nano-rods alongside spherical particles suggests a mixed growth mechanism influenced by the synthesis conditions (Wang et al., 2014; Al-Mulla et al., 2024). In conjunction with the green reducing agent, the sonication process promotes the nucleation and growth of different morphological structures under
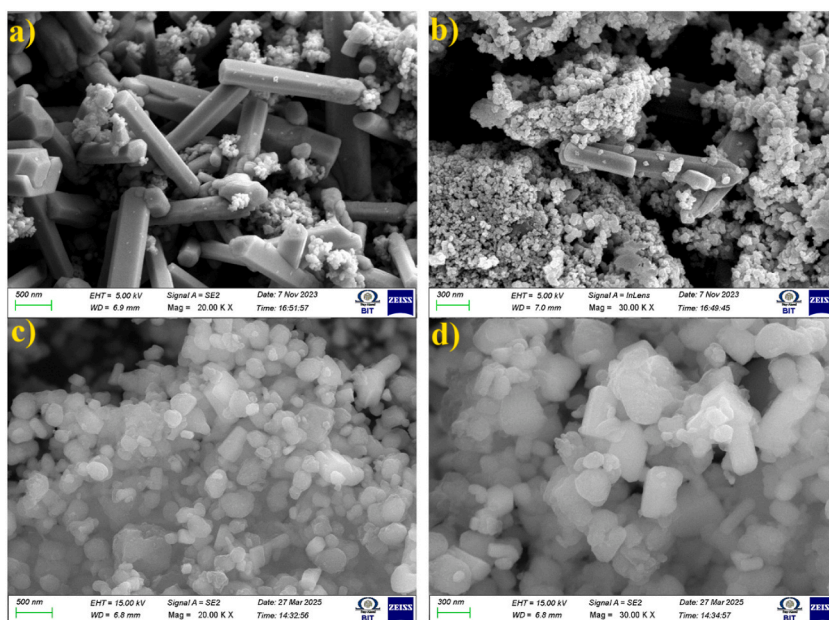
Fig. 3. FESEM images of prepared ZnO-S (a–b) and ZnO-N (c–d) nanoparticles at various magnifications.

specific conditions (Karthikeyan et al., 2023a). The coexistence of spherical and hexagonal structures can be attributed to the dynamic nature of the sonication approach, which provides varying energy inputs that facilitate the formation of multiple morphologies. The hexagonal nano-rods indicate anisotropic growth, a characteristic feature of ZnO crystallization under specific synthesis parameters. The morphological diversity observed in the FESEM analysis can have significant implications for the functional properties of the ZnO NPs.

Similarly, the FESEM image of ZnO-N as depicted in Fig. 3(c–d) revealed non-uniform spherical and cubical structures of ZnO NPs. The morphology included well-dispersed structures effectively due to the reducing role played by NaOH. However, minor agglomeration observed in the sample can be attributed to either the absence of a stabilizing agent or the sonication approach, creating a high surface charge over the particles. In addition, the FESEM image corresponded with the increased particle size observed in PSA analysis, possibly due to the chemical reducing agent. In comparison, the green synthesis sample produces well-structured nanoparticles with reduced particle size.

3.3. Functional group analysis

FTIR was employed to characterize the synthesized ZnO NPs functional groups and bonding environments. As seen in Fig. 4, the FTIR spectrum of ZnO-S samples exhibited distinct peaks at wave numbers 3474, 1624, 1449, 1110, and 618 cm^{-1}, each providing insights into the nanoparticles' chemical composition and surface characteristics. The peak observed at 3474 cm^{-1} corresponds to the O-H stretching vibration, indicating hydroxyl groups (Raj and Lawerence, 2018). This peak suggested the presence of hydroxyl groups on the surface of the ZnO-S NPs, likely resulting from adsorbed water or surface hydroxylation during the synthesis process. The presence of this peak highlighted the hydrophilic nature of the nanoparticles' surface, which can influence their interaction with aqueous environments and their overall stability. At 1624 cm^{-1}, the spectrum showed a peak associated with C=C stretching vibrations commonly found in organic compounds or carbon residues (Jha et al., 2023; Pham et al., 2022). This peak may arise from residual organic material originating from the *S. ovata* extract used in the nanoparticle synthesis. This observation suggested that the ZnO-S NPs may interact with organic components in the extract, indicating potential surface modifications or capping effects. The peak at 1449 cm^{-1} represents C-H bending vibrations, characteristic of aliphatic hydrocarbons (Pham et al., 2023). The presence of this peak suggested that there may be residual aliphatic carbon components from the phytochemical residues or capping agents used during synthesis. This further implied that the extract may play a role in stabilizing the nanoparticles through organic interactions. Another notable peak at 1110 cm^{-1} is attributed to C-O stretching vibrations, which could be related to carboxyl or ester groups (Doan Thi et al., 2020). This peak indicated possible interactions between the ZnO-S NPs and the organic moieties from the *S. ovata* extract, reinforcing the extract's role in stabilizing and capping the nanoparticles. Finally, the peak at 618 cm^{-1} is characteristic of Zn-O stretching vibrations, confirming the presence of ZnO in the nanoparticles (Ramesh et al., 2015; Tan et al., 2023). This peak validated the successful synthesis of ZnO-S NPs through the green synthesis approach.

Similarly, the ZnO-N samples show prominent functional group peaks at 3426, 1614, 1395, and 638 cm-1. The presence of peaks at 1614 and 3426 cm^{-1} can be attributed to the stretching and bending vibrations of O-H groups, possible due to the adsorption of moisture by KBr or samples. The additional peak at 1395 cm^{-1} is attributed to the strong stretching vibration of C=O, possibly due to the CO_2 adsorption on the surface of the molecules. Furthermore, a strong peak at 638 cm-1 confirms the presence of ZnO, corresponding to the Zn-O peak. The presence of this peak serves as a definitive marker of the ZnO phase in the synthesized material. Following XRD, the absence of additional peaks in the FTIR spectrum indicates that the synthesis process has yielded high-purity ZnO NPs.
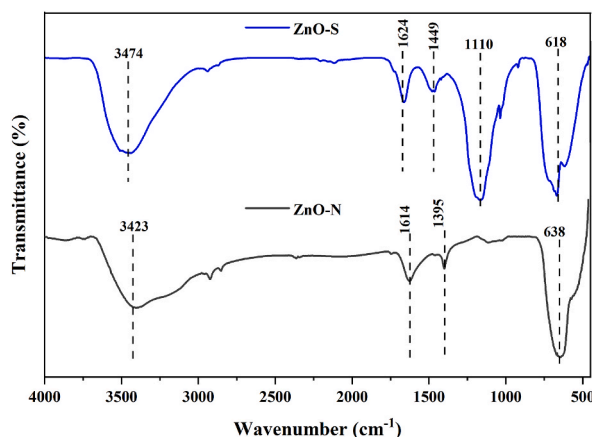

Fig. 4. FTIR spectra of prepared ZnO NPs.

3.4. Particle size analysis

The particle size distribution of the synthesized ZnO NPs reveals their size characteristics and uniformity, as seen in Fig. 5. The particle size data are represented by the d-values, which denote the diameters at which 10 %, 50 %, and 90 % of the particles fall below, respectively. For ZnO-S samples, the particle size d_{10}, d_{50}, and d_{90} values are 4.05, 33.84, and 119.79 nm. In contrast, the particle size d_{10}, d_{50}, and d_{90} values for the prepared ZnO-N sample are 15.96, 81.2, and 612.54 nm, respectively. The smaller average particle size of the prepared ZnO-S sample than ZnO-N can be attributed to the faster nucleation and growth, and reduced particle size through the green reducing agent. The smaller particle size of the prepared ZnO-S sample comparatively increases the surface area of particles, improving higher reactive sites for catalytic applications.

3.5. UV–Vis absorbance analysis

The optical properties of the synthesized ZnO NPs were investigated using UV–Vis spectroscopy, as shown in Fig. 6 (a). The UV–Vis spectrum displays a distinct absorption peak at 369 and 378 nm for ZnO-S and ZnO-N NPs, indicating the characteristic absorption edge of ZnO nanoparticles. The maximum absorbance observed can be attributed to the electronic transition from the valence band to the conduction band, corresponding to the prominent ZnO's broadband gap semiconductor properties (Bu and Huang, 2015). This absorption peak is consistent with the band gap energy of ZnO, affirming the successful synthesis of ZnO NPs with desired optical properties. A slight blue shift of ZnO-S compared with ZnO-N NPs can be ascribed to the lower particle size, which significantly increases the material's band gap. The optical band gap (Eg) was calculated using the Tauc plot method to analyze the optical properties further. The Tauc plot equation is given by (Santika et al., 2024):

$$(\alpha h\nu)^2 = A\left(h\nu - E_g\right)$$

Where α is the absorption coefficient, $h\nu$ is the photon energy, A is a constant, and Eg is the optical band gap. By plotting $(\alpha h\nu)$ against $h\nu$ and extrapolating the linear portion of the curve to the photon energy axis, the direct band gap energy of the ZnO-S and ZnO-N NPs was determined to be 3.2 eV and 2.89 eV, as shown in Fig. 6 (b). The increased band gap of the ZnO-S NPs can be attributed to the observed blue shift in absorption spectra due to the lower particle size effects leading to quantum confinement effects (Debanath and Karmakar, 2013; Hadi et al., 2014; Kumar and Rao, 2015).

3.6. Thermogravimetric analysis

The TGA curves of prepared ZnO NPs are shown in Fig. 7. The TGA curves of prepared ZnO-S NPs show a two-stage weight loss. Initial stage weight loss occurs between 30 and 400 °C, possibly due to the degradation of volatile organic compounds and attached surface groups. The sample remains stable till 800 °C, and a prominent weight loss was observed after 800 °C, possible due to the decomposition of inorganic molecules. The total weight loss for the ZnO-S is 10.31 %. Similarly, for ZnO-N NPs, the first stage weight loss for the ZnO-N sample occurs between the 30–300 °C temperature range, eliminating volatile molecules and surface-attached water molecules. The stability of the particle remained till 800 °C, and inorganic decomposition occurred between 800 and 1000 °C. The total weight loss with the prepared ZnO-N samples is 12.91 %. A slight increase in the thermal stability can be observed with the green synthesized samples. This can be attributed that the bioactive compounds in these extracts, such as polyphenols and flavonoids, act as stabilizing and capping agents, preventing aggregation and enhancing the nanoparticles' resistance to high temperatures (Jayasimha et al., 2024).
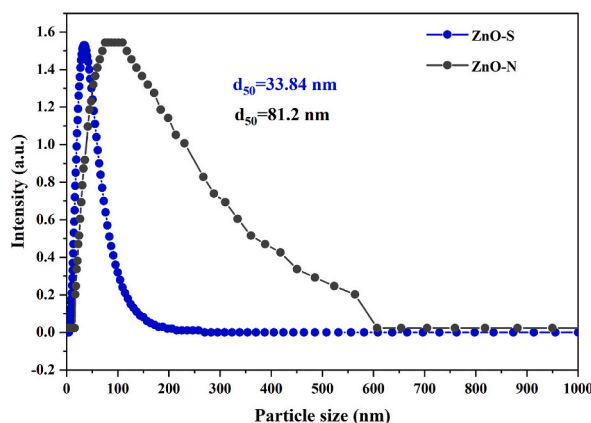

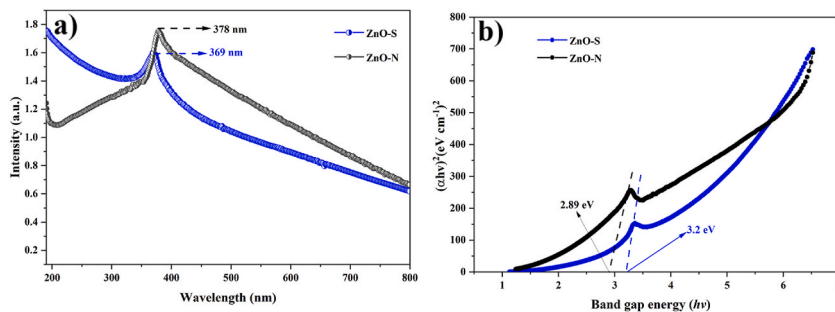**Fig. 5.** Particle size of prepared ZnO NPs.

Fig. 6. Optical properties of prepared ZnO NPs a) UV–Vis spectra and b) optical band gap.
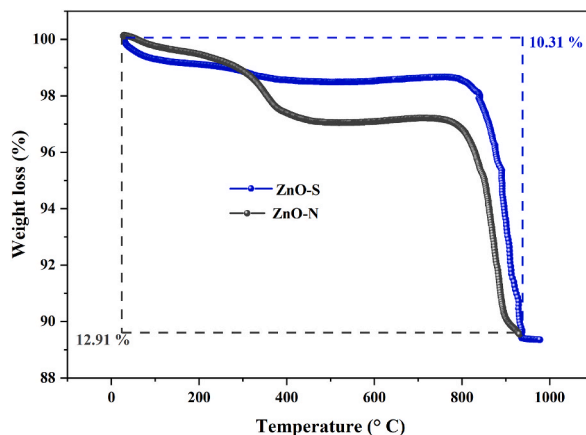

Fig. 7. TGA and DTA curve for prepared ZnO NPs.

3.7. BET surface analysis

The surface area of ZnO NPs plays a significant role, adding photocatalytic and antimicrobial activities to the surface properties of the particles. Brunauer–Emmett–Teller (BET) gas sorption measurements were applied on ZnO NPs, where the nitrogen adsorption-desorption process characterized the specific surface area and mesoporous features of the ZnO-S and ZnO-N NPs at 77 K. As shown in Fig. 8, ZnO NPs exhibit a type IV isotherm. After utilizing the Barrett–Joyner–Halenda (BJH) method, nitrogen desorption determined mesopore sizes, while the cumulative volume of pores was calculated as pore volume. As shown in Fig. 8 (a), the bio-fabricated ZnO-S NPs show surface area, pore volume, and pore diameter of 72.367 m^2/g, 0.391 cc/g, and 14.415 nm, respectively. Similarly, for ZnO-N NPs, the observed surface area, pore volume, and pore diameter are 84.251 m^2/g, 7.498 cc/g, and 8.24 nm. The increased surface area of ZnO-N nanoparticles can be ascribed to the observed spherical and cubic morphology, offering a slightly higher surface area than the nanorod morphology of ZnO-S samples. However, larger pore diameters observed in ZnO-S samples generally increase the surface area available for reactions, improve the diffusion of reactants and products, allow deeper light penetration to activate
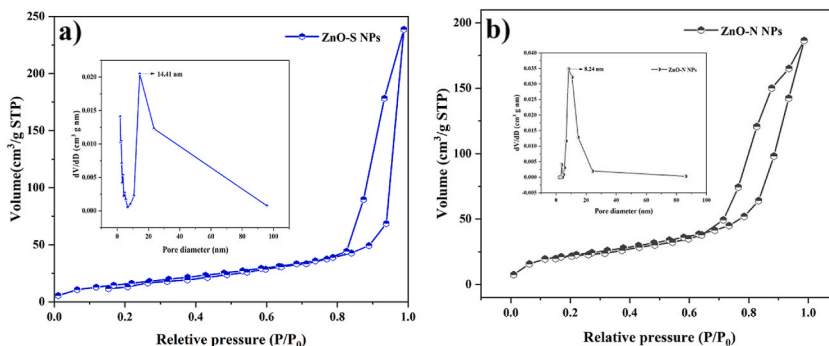

Fig. 8. BET analysis of a) ZnO-S and b) ZnO-N NPs.

more sites, enhance the adsorption of reactant molecules, reduce the electron-hole recombination rate, and induce photocatalytic activity.

3.8. Antioxidant activity

This study investigated the antioxidant, antibacterial, and photocatalytic activities of the NPs. Key parameters such as crystallite size, particle size, morphological structure, surface area, and band gap are recognized as critical determinants influencing their potential applications. The green-synthesized ZnO NPs (ZnO-S) demonstrated superior performance when compared to their chemically synthesized counterparts. Specifically, XRD analysis revealed a reduced crystallite size, while FESEM confirmed the formation of distinctive nanorod-like structures. Furthermore, the ZnO-S samples exhibited enhanced thermal stability. Notably, the increased band gap observed in ZnO-S is associated with a lower electron hole recombination rate, thereby promoting higher reactive oxygen species (ROS) generation, an essential mechanism for antibacterial and photocatalytic activities. Additionally, incorporating functional groups from *S. ovata* significantly enhanced the antioxidant potential of the ZnO-S samples. Consequently, the application-based investigations in this study were conducted exclusively on the green-synthesized ZnO NPs.

As illustrated in Fig. 9, the antioxidant activity of the ZnO-S NPs synthesized using *S. ovata* was evaluated based on their ability to scavenge free radicals, with results indicating varying degrees of effectiveness at different concentrations. The data demonstrated a concentration-dependent increase in antioxidant activity for ZnO-S NPs and *S. ovata* powder. At the lowest concentration tested (25 μg/mL), the ZnO-S NPs exhibited about 2-fold higher free radical scavenging percentage (53.88 %) than *S. ovata* powder (25 %). This suggested that the nanoparticles have a relatively higher antioxidant effect at this concentration. As the concentration increased to 50 μg/mL, the antioxidant activity of the ZnO-S NPs improved significantly to 78.15 %, while the *S. ovata* showed a scavenging percentage of 69.75 %. This demonstrated that the ZnO-S nanoparticles become increasingly effective at neutralizing free radicals at higher concentrations, outperforming the natural extract. At 100 μg/mL concentration, the ZnO-S NPs demonstrated an impressive scavenging percentage of 92.12 %, slightly higher than the 89.45 % observed for the *S. ovata*. The finding underscored the enhanced antioxidant efficacy of ZnO-S NPs at higher concentrations, rivaling and potentially surpassing that of the natural extract. The antioxidant activity of ZnO-S NPs significantly surpasses that of *S. ovata* across all tested doses, indicating the nanoparticles' considerable potential as effective free radical scavengers. The concentration-dependent enhancement in antioxidant activity underscores the efficacy of ZnO-S NPs in combating oxidative stress. It suggests their potential utility in various applications, including biomedical and environmental contexts.

3.9. Antibacterial activity

The antibacterial activity of the synthesized ZnO-S NPs was evaluated against *E. coli* and *S. aureus* at concentrations of 25, 50, and 100 mg/mL. The zones of inhibition were measured to assess the effectiveness of the ZnO-S NPs, and the results were compared with the standard antimicrobial agent, streptomycin (S25), at 25 mg/mL. The observed results are illustrated in Fig. 10 and summarized in Table 2. For *E. coli*, the ZnO-S NPs exhibited increasing antibacterial activity with higher concentrations. At 25 mg/mL, the zone of inhibition was 15 mm, which improved to 18 mm at 50 mg/mL and increased to 20 mm at 100 mg/mL. Streptomycin (25 mg/mL) demonstrated a zone of inhibition of 12 mm, serving as a reference.

Similarly, for *S. aureus*, the inhibition zones increased with the concentration of ZnO-S NPs. At 25 mg/mL, the inhibition zone was 19 mm, growing to 21 mm at 50 mg/mL and reaching 23 mm at 100 mg/mL. Streptomycin (25 mg/mL) produced a zone of inhibition of 15 mm. The data reveal that ZnO-S NPs exhibit more pronounced inhibition against *S. aureus* (Gram-positive) than *E. coli* (Gram-negative). This is attributed to the structural differences between bacterial types. Gram-positive bacteria have a thick peptidoglycan layer in their cell walls, which is more susceptible to the penetration and antimicrobial effects of ZnO-S NPs. (Azam et al., 2012).

In contrast, Gram-negative bacteria possess an additional outer membrane that acts as a barrier, reducing the penetration of nanoparticles and antimicrobial agents (Azam et al., 2012). ZnO-S NPs exhibit potent antibacterial activity, which is primarily
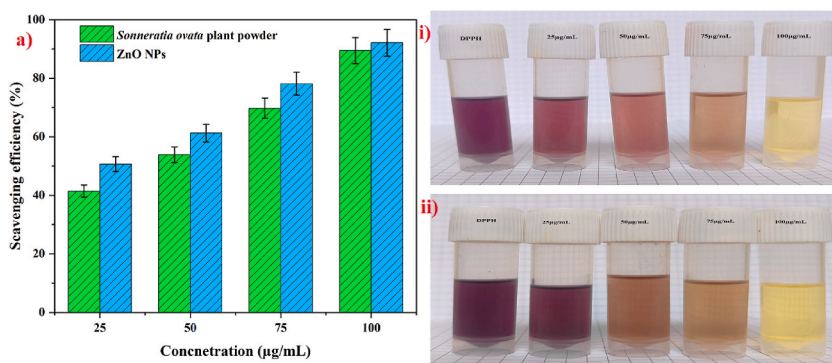
Fig. 9. DPPH scavenging potential of *S. ovata* and ZnO-S NPs at various concentrations and decolorization of DPPH i) *S. ovata* plant powder, and ii) ZnO-S NPs.
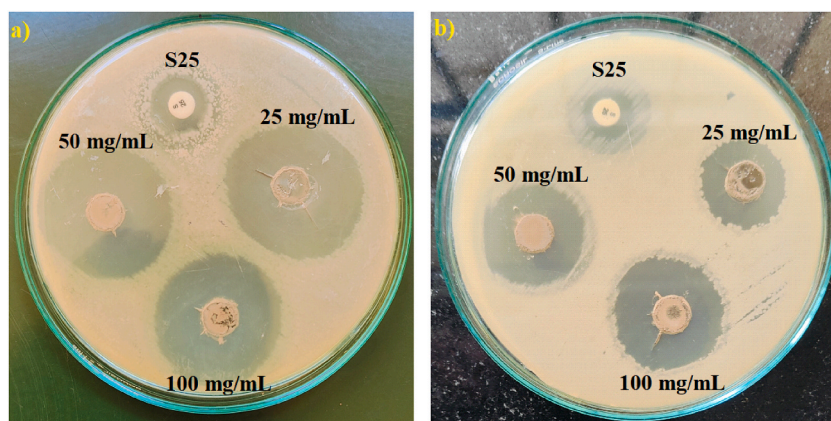
Fig. 10. Antibacterial activity of prepared ZnO-S NPs against a) *S. aureus* and b) *E. coli*.

Table 2
The zone of inhibition formed by ZnO-S NPs.

Sample	Zone of inhibition (mm)							
	Staphylococcus aureus				*Escherichia coli*			
	S25	25	50	100	S25	25	50	100
ZnO-S NPs	15 ± 0.075	19 ± 1.05	21 ± 1.05	23 ± 1.15	12 ± 0.6	15 ± 0.75	18 ± 0.9	20 ± 1

attributed to their ability to generate reactive oxygen species (ROS) such as hydroxyl radicals, hydrogen peroxide, and superoxide anions. These reactive molecules induce oxidative stress in bacterial cells, damaging cellular components such as lipids, proteins, and DNA, ultimately leading to cell death. Additionally, ZnO-S NPs can directly interact with the bacterial cell membrane, causing structural disruptions due to their sharp edges and high surface-to-volume ratio. This interaction can lead to increased cell permeability, resulting in the leakage of vital cellular contents (Agarwal et al., 2018). Furthermore, ZnO-S NPs can disrupt bacterial metabolic processes by releasing zinc ions, which can interfere with enzymatic systems inside the cell, inhibiting growth and proliferation. Combining these mechanisms makes ZnO-S NPs highly effective as antibacterial agents against many bacterial pathogens. (Yin et al., 2020; Shi et al., 2014). In Gram-positive bacteria, the damage to the peptidoglycan layer and cytoplasmic membrane results in cell lysis and death. The ROS can also disrupt the outer membrane of Gram-negative bacteria, leading to increased permeability and subsequent bacterial cell death.

3.10. Photocatalytic activity

Optimizing various parameters, including catalyst concentration, dye concentration, and pH levels, was employed to investigate the photocatalytic degradation of EtBr loaded with synthesized ZnO-S nanocatalyst. UV–Vis spectroscopy was employed to measure the absorbance of the model pollutant solution containing the ZnO-S nanocatalyst within the wavelength range of 190–600 nm. The maximum absorbance was observed at 285 nm. For absorbance measurements, 5 mL aliquots of the dye solution were sampled, centrifuged, and analyzed at 15-min intervals over 120 min.

3.10.1. Effect of the catalyst

The effect of catalyst concentration on the degradation of a 10-ppm EtBr solution was studied using ZnO-S nanocatalyst loadings of 100, 200, 300, and 400 ppm. As shown in Fig. 11(a–d), the absorbance of the EtBr solution loaded with ZnO-S nanocatalyst significantly decreased over time, indicating the degradation of EtBr molecules. The degradation efficiencies for ZnO-S catalyst concentrations of 100, 200, 300, and 400 ppm were 73.4 %, 76.8 %, 89.4 %, and 84.73 %, respectively. The observed increase in degradation efficiency from 100 to 300 ppm can be significantly attributed to the increased photon absorption by the catalyst at higher concentrations. This phenomenon enhances the photocatalytic activity as more photons are available to excite the electrons in the catalyst, leading to greater generation of ROS (Saber et al., 2024). With increasing catalyst loading, there is a corresponding rise in the number of photon absorption centers and active sites on the catalyst surface, significantly enhancing the degradation of EtBr molecules (Ye et al., 2018). However, the degradation efficiency decreased at a catalyst concentration of 400 ppm. The drop in efficiency at higher catalyst concentrations is likely due to the agglomeration of nanocatalyst particles, which diminishes the effective surface area essential for catalytic activity and limits the exposure of reactive sites necessary for catalytic reactions.

Additionally, excessive catalyst loading can increase light scattering and shielding effects, thereby reducing light penetration through the solution and decreasing the overall photocatalytic activity (Zhang et al., 2020). Therefore, optimizing the catalyst loading
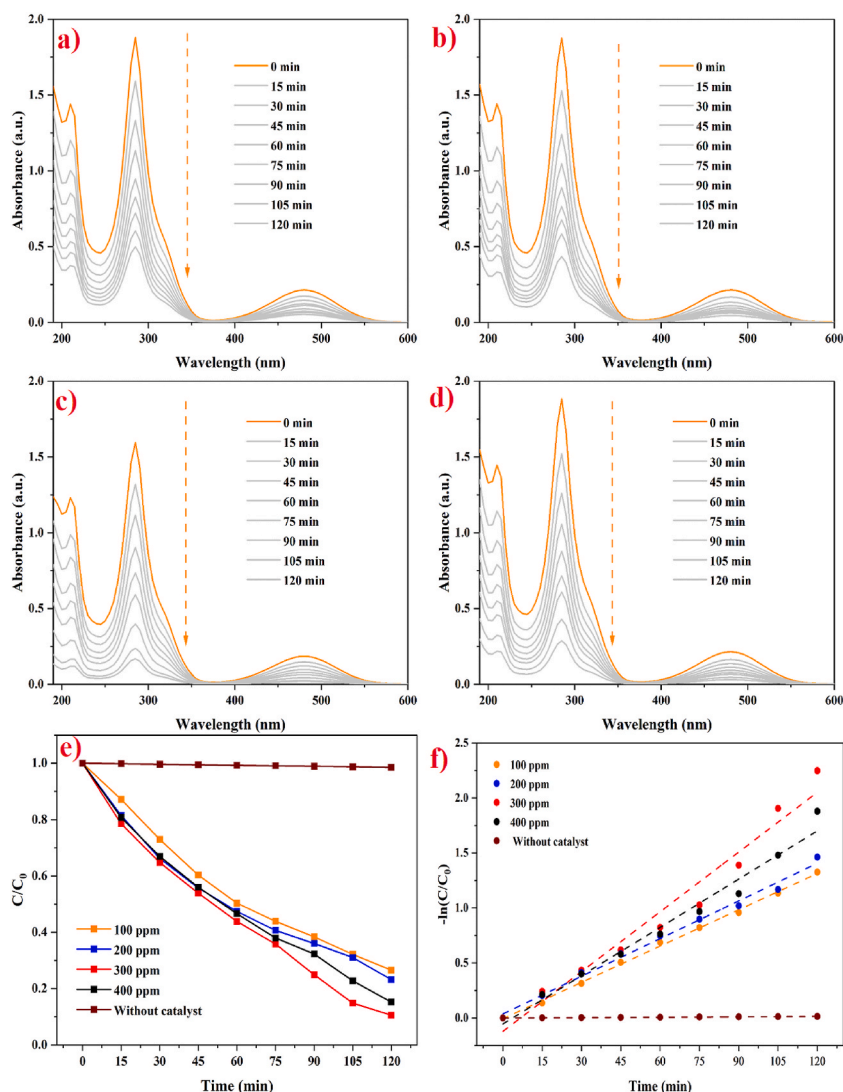
Fig. 11. Absorbance spectra of EtBr solution loaded with various concentrations of ZnO-S nanocatalyst a) 100, b) 200, c) 300, and d) 400 ppm—Pseudo first-order degradation kinetic outcomes e) C/C0 curve and d) kinetic rate curve.

concentration is crucial to avoid catalyst wastage and prevent degradation loss due to catalyst agglomeration. Furthermore, a pseudo-first-order kinetic model was employed to determine the EtBr solution's degradation rate using the synthesized ZnO-S nanocatalyst. The C/C_0 curve, depicting the effect of catalyst concentration on the degradation of the EtBr solution, is provided in Fig. 11(e). As shown in Fig. 11(f), the kinetic relationship between catalyst concentration and degradation of the EtBr solution is observed to increase linearly with time. The degradation rates of the EtBr solution with different concentrations of ZnO-S nanocatalyst are provided in Table 3. These rate constants offer insight into the efficiency of the photocatalytic process at varying catalyst loadings. The optimal ZnO-S nanocatalyst concentration of 300 ppm was selected for further optimization, including determining the effects of dye concentration and pH levels.

Table 3
Rate of EtBr degradation with different concentrations of ZnO-S nanocatalyst at dye concentration (10 ppm).

Sample concentration (ppm)	Degradation efficiency (%)	Rate of the reaction (x min^{-1})	R^2
ZnO-S (100 ppm)	73.43	1.11×10^{-2}	0.998
ZnO-S (200 ppm)	76.82	1.14×10^{-2}	0.992
ZnO-S (300 ppm)	89.43	1.81×10^{-2}	0.964
ZnO-S (400 ppm)	84.73	1.46×10^{-2}	0.978

3.10.2. Effect of dye concentration

The effect of dye concentration on the fixed ZnO-S catalyst concentration (30 ppm) was studied with different dye concentrations such as 20, 30, 40, and 50 ppm. The absorbance graphs of varying dye concentrations are shown in Fig. 12(a–d). The degradation efficiency of 20, 30, 40, and 50 ppm concentrations was 88.54, 86.98, 83.45, and 79.79 %, respectively. The degradation efficiency gradually decreased with the increase in dye concentration. This can be associated with different factors initially; the ZnO-S catalyst has a finite number of active sites available for photocatalytic reactions. At higher EtBr concentrations, the number of EtBr molecules exceeds the number of available active sites on the catalyst surface, decreasing relative degradation efficiency (Daneshvar et al., 2003). There are insufficient active sites to accommodate all the EtBr molecules, resulting in less efficient degradation. Higher concentrations of EtBr can lead to the accumulation of intermediate degradation products. These intermediates can compete with EtBr molecules for active sites on the catalyst surface, reducing the overall degradation efficiency. The C/C_0 curve, represented in Fig. 12 (e), shows the gradual decrease in the pollutant over an increase in time and comparison of different dye concentrations employed. Additionally, the pseudo-first degradation kinetic relation, as seen in Fig. 12 (f), clearly illustrates the reaction rate for various concentrations of dyes. The response rate from Table 4 demonstrated that the degradation rate of 50 ppm dye concentration is reduced by 1.32 times compared to 20 ppm dye concentration. To perform optimal degradation, a 30-ppm dye concentration was selected to analyze the change in degradation concerning different pH levels.

3.10.3. Effect of pH

To study the effect of pH on the degradation of an EtBr solution, an optimized dye concentration of 30 ppm and a ZnO-S
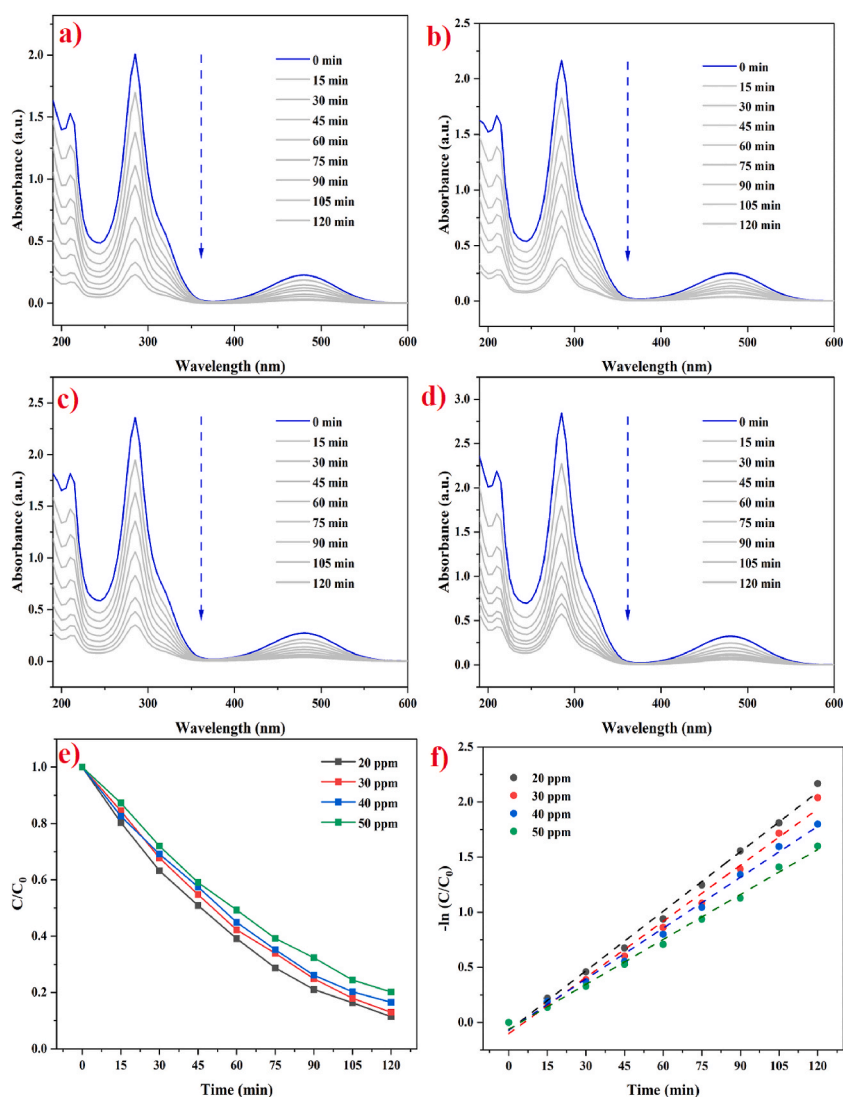
Fig. 12. UV spectra of different dye concentrations applied to a fixed ZnO-S nanocatalyst concentration (300 ppm): a) 20 ppm, b) 30 ppm, c) 40 ppm, d) 50 ppm. Additionally, e) C/C_0 curve, and f) kinetic relation for the specific operational parameter.

Table 4

Degradation kinetic rate of different concentrations of EtBr over constant ZnO-S catalyst concentration (300 ppm).

Dye Concentration (ppm)	Degradation efficiency (%)	Rate of Reaction (x min^{-1})	R^2
EtBr (20 ppm)	88.54	1.81×10^{-2}	0.995
EtBr (30 ppm)	86.98	1.69×10^{-2}	0.990
EtBr (40 ppm)	83.45	1.53×10^{-2}	0.994
EtBr (50 ppm)	79.79	1.35×10^{-2}	0.995

nanocatalyst concentration of 30 ppm were employed. Initially, the pH of the 30 ppm EtBr dye solution was 7.1. The pH of the solution was first adjusted to 5. The absorbance graph for the pH 5 solution, as seen in Fig. 13, shows a degradation efficiency of 75.7 %, which is lower than that at pH 7.1. This reduction in efficiency can be attributed to the surface charge effects of EtBr and the ZnO-S nanocatalyst. Previous literature shows that EtBr and ZnO-S nanoparticles exhibit positive surface charge characteristics (Bhattacharya and Mandal, 1997; Heibati et al., 2016; Kim et al., 2014; Baek et al., 2011). In an acidic solution, the positive charge of the ZnO-S nanocatalyst is enhanced, leading to repulsion between the ZnO-S nanocatalyst and EtBr molecules, thereby reducing the degradation efficiency.

The pH levels of the solution were subsequently adjusted to 9, 11, and 13. The absorbance graphs for these pH levels are provided in Fig.s 13(b), 13(c), and 13(d), respectively. The degradation efficiency significantly increased to 87.6 % at pH 9 and 98.6 % at pH 11.
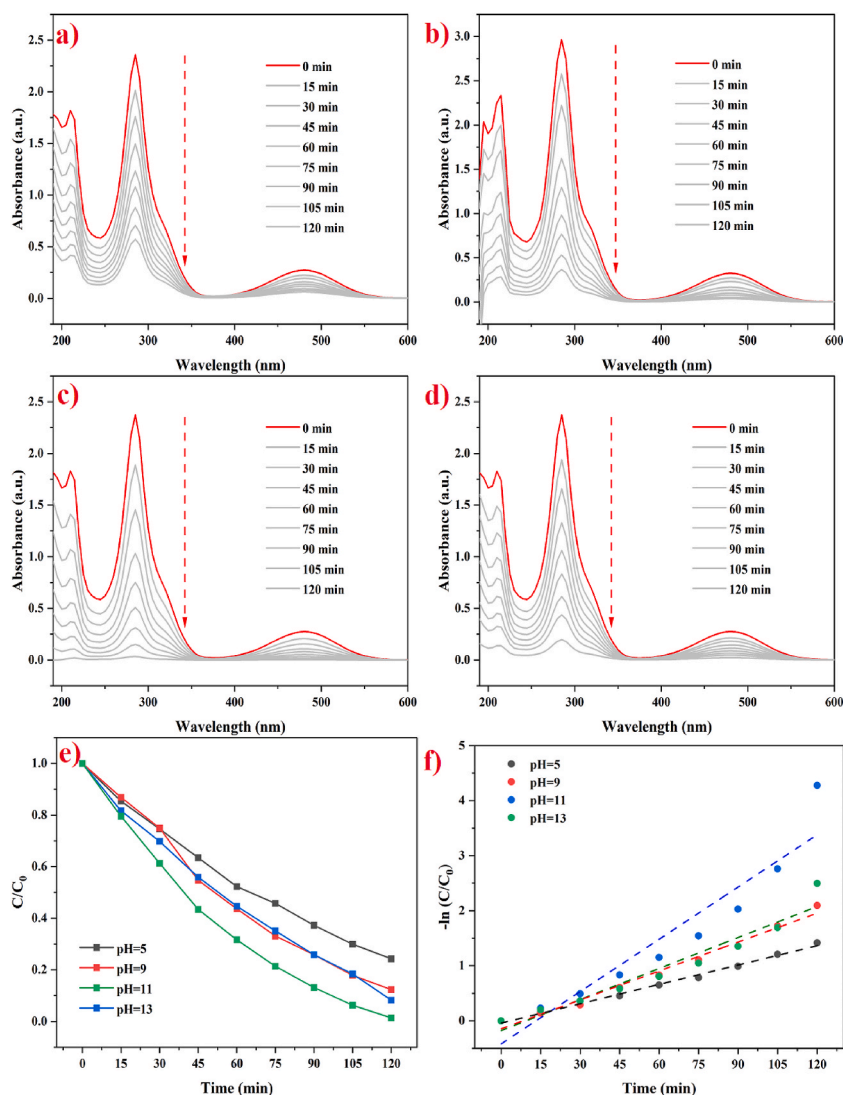
Fig. 13. Absorbance of EtBr degradation at different pH levels such as a) pH = 5, b) pH = 9, c) pH = 11, and d) pH = 13. Further, e) C/C0 curve and f) Kinetic curve for the different pH operational parameters of EtBr solution with ZnO-S nanocatalyst.
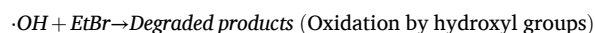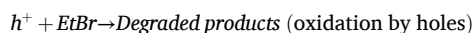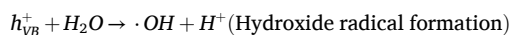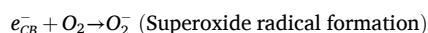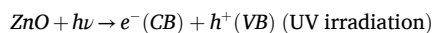
This improvement can be attributed to the change in surface charge characteristics of the ZnO-S catalyst from neutral to negative, which enhances the attraction between the ZnO-S nanocatalyst and EtBr molecules, thereby increasing degradation efficiency. However, the degradation efficiency decreased to 91.74 % at pH 13. This reduction can be attributed to the partial dissolution of the ZnO-S nanocatalyst at higher pH levels, which inhibits its effective performance and consequently reduces the degradation efficiency of EtBr. The C/C_0 curve and kinetic relation of ZnO-S nanocatalyst with EtBr solution at different pH levels are provided in Fig.s 13 (e) and X(f), respectively. As shown in Table 5, the kinetic rate of the EtBr solution at pH 11 is approximately 1.9 times higher than that of the solution at pH 7.1, with both having an EtBr concentration of 30 ppm and ZnO-S nanocatalyst concentration of 30 ppm.

Several key factors, including the concentration of the catalyst, the concentration of the dye, and the pH of the solution significantly influence the efficiency of EtBr degradation. By carefully optimizing these parameters, the photocatalytic degradation process can be markedly enhanced, leading to improved performance of the ZnO-S nanocatalyst in environmental remediation applications. This optimization ensures that the nanocatalyst operates under ideal conditions, maximizing its ability to break down contaminants effectively and contributing to more efficient pollution control. The comparative analysis of various pollutant and green synthesis agents is provided in Table 6.

3.11. Degradation mechanism

The possible photocatalytic degradation mechanism of ZnO-S NPs with an EtBr solution involves several key steps: light absorption, generation of electron-hole pairs, formation of ROS, and the eventual degradation of EtBr molecules (Majumder et al., 2020; Karthikeyan et al., 2023b). As seen in Fig. 14, when the ZnO-S nanoparticles are exposed to UV light with energy greater than or equal to their bandgap energy (~3.37 eV for ZnO-S), electrons (e^-) in the valence band (VB) are excited to the conduction band (CB), leaving behind holes (h^+) in the VB (Silva et al., 2016). The photoexcited electrons and holes migrate to the surface of the ZnO-S NPs, participating in redox reactions. Effective charge separation is crucial for high photocatalytic efficiency, as recombination of e^- and h^+ can lead to energy loss without generating reactive species. The electrons and holes generated can react with molecular oxygen (O_2) and water (H_2O) to form ROS, such as superoxide radicals ($O_2^-\cdot$), hydroxyl radicals ($\cdot OH$), and hydrogen peroxide (H_2O_2) (Bechambi et al., 2015). The *S. ovata* leaf extract used in this study contains phytochemicals such as flavonoids and polyphenols, which are rich in hydroxyl, carbonyl, and carboxyl groups. These functional groups not only assist in the green synthesis of ZnO by reducing and capping zinc ions, but also remain adhered to the nanoparticle surface, modulating its electronic and surface properties. During photocatalytic degradation, these phytochemicals can enhance the adsorption of EtBr molecules through hydrogen bonding or π-π interactions. Furthermore, they may facilitate better separation of photoinduced electron–hole pairs by acting as surface electron sinks, thus increasing the generation of ROS such as $\bullet OH$ and $O_2^\bullet$, which are crucial for oxidative degradation of EtBr.

The ROS generated (especially hydroxyl radicals) are highly reactive and can degrade EtBr through oxidative reactions; breaking down its complex structure into smaller, less harmful molecules. The combined effect of direct oxidation by holes and indirect oxidation by ROS resulted in the degradation of EtBr. The overall reaction can be summarized as follows,

$ZnO + h\nu \rightarrow e^-(CB) + h^+(VB)$ (UV irradiation)

$e_{CB}^- + O_2 \rightarrow O_2^-$ (Superoxide radical formation)

$h_{VB}^+ + H_2O \rightarrow \cdot OH + H^+$ (Hydroxide radical formation)

$h^+ + EtBr \rightarrow Degraded\ products$ (oxidation by holes)

$\cdot OH + EtBr \rightarrow Degraded\ products$ (Oxidation by hydroxyl groups)

3.12. Cyclic stability

The cyclic stability of the ZnO-S nanocatalyst was rigorously assessed under optimized conditions: a dye concentration of 300 ppm, a catalyst concentration of 30 ppm, and a pH level of 11. This evaluation was conducted over five consecutive cycles to determine the photocatalytic durability of the catalyst, with the results detailed in Fig. 15. After the completion of five cycles, the photocatalytic degradation efficiency exhibited a slight reduction of 6.9 %. This modest decrease indicated the high stability and minimal loss in activity of the ZnO-S nanocatalyst, reinforcing its suitability for repeated use in environmental remediation. The retention of photocatalytic efficiency over multiple cycles underscored the robustness of the ZnO-S nanocatalyst, making it an economically viable option for long-term applications. Furthermore, the results suggested that the ZnO-S nanocatalyst possesses excellent structural and chemical stability under alkaline conditions, which is crucial for maintaining effectiveness in the continuous degradation of organic pollutants. This study confirmed the potential of the ZnO-S nanocatalyst to be a sustainable solution in water treatment technologies, providing a reliable method for the efficient and repeated removal of contaminants.

4. Conclusion

In this study, ZnO-S NPs were successfully synthesized using *Sonneratia ovata* extract; a green chemistry approach that offers an eco-friendly and sustainable method for nanoparticle production. The synthesized ZnO-S NPs were characterized through various

Table 5

Kinetic degradation rate of different pH levels of EtBr solution (300 ppm) with catalyst concentration of 30 ppm.

Solution pH	Degradation efficiency (%)	Rate of Reaction (x min^{-1})	R^2
pH = 5	75.75	1.17×10^{-2}	0.994
pH = 9	87.68	1.75×10^{-2}	0.983
pH = 11	98.61	3.16×10^{-2}	0.912
pH = 13	91.74	1.87×10^{-2}	0.938

Table 6

Comparative analysis of various green synthesis agents and pollutants using photocatalytic process.

Synthesis method	Photocatalyst	Pollutant	Irradiation Time (min)	Efficiency (%)	References
Sargassum muticum	ZnO	Methylene blue	60	96	Subramanian et al. (2021)
Ulva lactuca	ZnO	Methylene blue	120	95	Ishwarya et al. (2018)
Padina tetrastromatica	ZnO	Drimarene Turquoise Blue	180	99	Pandimurugan and Thambidurai (2016)
Mussaenda frondosa	ZnO	Methylene blue	100	90	Jayappa et al. (2020)
Chemicals	FeO	Ethidium bromide	240	98	Xie et al. (2021)
Chemicals	Mn - ZnS	Ethidium bromide bromide	360	98.1	Saruchi et al. (2020)
Chemicals	C - Fe - TiO2	Ethidium bromide	120	90	Lavand and Malghe (2016)
Chemicals	ZnO	Ethidium bromide	150	76	Biswal et al. (2021)
Sonneratia ovata leaves	ZnO	Ethidium bromide	120	98.61	This work
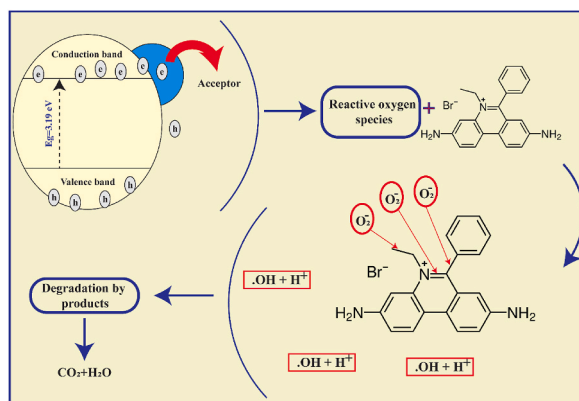
Fig. 14. The proposed degradation mechanism of EtBr pollutant involving the prepared ZnO-S NPs.
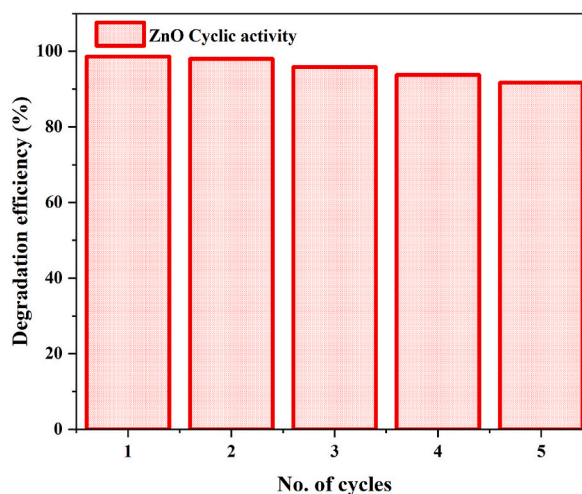
Fig. 15. Cyclic photocatalytic activity of the optimized system degradation efficiency for five cycles.

techniques to confirm their crystallographic, morphological, thermal, functional group, surface area, and optical properties compared to chemically prepared ZnO NPs. The XRD analysis confirmed the hexagonal wurtzite structure of ZnO-S NPs, with an average crystalline size of 24.6 nm. FTIR spectra showed the characteristic ZnO-S peaks, confirming the purity of the nanoparticles. FESEM images revealed predominantly spherical structures with occasional hexagonal nanorods, indicative of the morphology of the synthesized nanoparticles. TGA/DT analysis indicated a two-stage thermal decomposition, with a total weight loss of 10.6 % (up to 1000 °C), suggesting the thermal stability of the ZnO-S NPs. The superior physicochemical properties of the prepared ZnO-S NP were obtained successfully through the green reducing agent. The ZnO-S NPs exhibited significant antibacterial activity against *Escherichia coli* (Gram-negative) and *Staphylococcus aureus* (Gram-positive). The antibacterial activity was concentration-dependent, with higher concentrations of ZnO-S NPs showing larger inhibition zones. The results also revealed a more pronounced inhibition against Gram-positive bacteria, which can be attributed to their cell wall structure, which is more susceptible to nanoparticle penetration and damage. The photocatalytic degradation of EtBr was optimized by varying operational parameters such as ZnO-S NPs concentration, EtBr concentration, and pH levels. The ZnO-S NPs demonstrated excellent photocatalytic efficiency, with the highest degradation observed at a concentration of 300 ppm ZnO-S NPs, 30 ppm EtBr solution, and a pH of 11. The UV–Vis spectroscopy measurements showed a significant decrease in absorbance at 285 nm, confirming the effective degradation of EtBr under UV irradiation.

CRediT authorship contribution statement

Kalidasan K: Writing – review & editing, Writing – original draft, Investigation. **Chavanich S:** Supervision, Investigation. **K.S.G. Jagan:** Resources, Methodology, Investigation. **Surendhiran S:** Methodology, Investigation, Data curation. **Naren Vidaarth T.M.:** Methodology, Investigation, Formal analysis, Data curation. **Karthik S:** Writing – review & editing, Resources, Methodology. **Kathiresan K:** Writing – review & editing, Resources. **Jean Wan Hong Yong:** Writing – review & editing, Resources, Funding acquisition. **Viyakarn V:** Writing – review & editing, Supervision, Project administration, Funding acquisition.

Funding

Declaration of competing interest

The authors declare that they have no known competing financial interests or personal relationships that could have appeared to influence the work reported in this paper.

Acknowledgments

Data availability

Data will be made available on request.

References

Abdel-Salam, O.M.E., Khadrawy, Y.A., Mohammed, N.A., 2012. Neuroprotective effect of nitric oxide donor isosorbide-dinitrate against oxidative stress induced by ethidium bromide in rat brain. EXCLI J 11, 125–141. https://pmc.ncbi.nlm.nih.gov/articles/PMC4932883/.

Abuzeid, H.M., Julien, C.M., Zhu, L., Hashem, A.M., 2023. Green synthesis of nanoparticles and their energy storage, environmental, and biomedical applications. Crystals (Basel) 13, 1576. https://doi.org/10.3390/cryst13111576.

Adán, C., Martínez-Arias, A., Fernández-García, M., Bahamonde, A., 2007. Photocatalytic degradation of ethidium bromide over Titania in aqueous solutions. Appl. Catal., B 76, 395–402. https://doi.org/10.1016/j.apcatb.2007.06.013.

Agarwal, H., Menon, S., Venkat Kumar, S., Rajeshkumar, S., 2018. Mechanistic study on antibacterial action of zinc oxide nanoparticles synthesized using green route. Chem. Biol. Interact. 286, 60–70. https://doi.org/10.1016/j.cbi.2018.03.008.

Al-Mulla, B.H., Abdulelah, H., Nawabjan, A., Hussin, S.M., Irfan, A., Ferdous Rahman, M., 2024. Fabrication and analysis of ZnO-S nanoflower and nanorod structures to improve superhydrophobicity using myristic acid. Results Phys. 67, 108051. https://doi.org/10.1016/j.rinp.2024.108051.

Almenia, S.H., Ismail, A.A., Alzahrani, K.A., Aljahdali, M., 2023. Design of mesoporous heterojunction CuCo$_2$O$_4$/Co$_3$O$_4$ photocatalyst with superior photocatalytic degradation of tetracycline. J. Photochem. Photobiol. Chem. 438, 114507. https://doi.org/10.1016/j.jphotochem.2022.114507.

Arrasheed, E.A., Meaz, T.M., Shalaby, R.M., Salem, B.I., Hemeda, O.M., Henaish, A.M.A., 2021. Rietveld refinement, cation distribution, morphological and magnetic study of NiAlxFe2-XO4 nanoparticles. Appl. Phys. A Mater. Sci. Process. 127. https://doi.org/10.1007/s00339-021-04360-9.

Astuti, M.D., Rosyidah, K., Umaningrum, D., Ardiyanti, R., Johan Abd Rasyied, H., Azzahra, A.P., 2023. The antioxidant activity and total phenolic content of *Sonneratia ovata* Back. Malays. J. Fundam. Appl. Sci. 19, 215–218. https://doi.org/10.11113/mjfas.v19n2.2789.

Azam, A., Ahmed, A.S., Oves, M., Khan, M.S., Habib, S.S., Memic, A., 2012. Antimicrobial activity of metal oxide nanoparticles against gram-positive and gram-negative bacteria: a comparative study. Int. J. Nanomed. 7, 6003–6009. https://doi.org/10.2147/IJN.S35347.

Baek, M., Kim, M.K., Cho, H.J., Lee, J.A., Yu, J., Chung, H.E., Choi, S.J., 2011. Factors influencing the cytotoxicity of zinc oxide nanoparticles: particle size and surface charge. J. Phys. Conf. Ser. 304, 012044. https://doi.org/10.1088/1742-6596/304/1/012044.

Bandeira, M., Giovanela, M., Roesch-Ely, M., Devine, D.M., da Silva Crespo, J., 2020. Green synthesis of zinc oxide nanoparticles: a review of the synthesis methodology and mechanism of formation. Sustain. Chem. Pharm. 15, 100223. https://doi.org/10.1016/j.scp.2020.100223.

Bechambi, O., Sayadi, S., Najjar, W., 2015. Photocatalytic degradation of bisphenol A in the presence of C-doped ZnO-S: effect of operational parameters and photodegradation mechanism. J. Ind. Eng. Chem. 32, 201–210. https://doi.org/10.1016/j.jiec.2015.08.017.

Bhattacharya, S., Mandal, S.S., 1997. Interaction of surfactants with DNA. Role of hydrophobicity and surface charge on intercalation and DNA melting. Biochim. Biophys. Acta 1323, 29–44. https://doi.org/10.1016/s0005-2736(96)00171-x.

Biswal, H.J., Yadav, A., Vundavilli, P.R., Gupta, A., 2021. High aspect ZnO-S nanorod growth over electrodeposited tubes for photocatalytic degradation of EtBr dye. RSC Adv. 11, 1623–1634. https://doi.org/10.1039/d0ra08124h.

Bu, I.Y.Y., Huang, R., 2015. One-pot synthesis of ZnO-S/reduced graphene oxide nanocomposite for supercapacitor applications. Mater. Sci. Semicond. Process. 31, 131–138. https://doi.org/10.1016/j.mssp.2014.11.037.

Daneshvar, N., Salari, D., Khataee, A.R., 2003. Photocatalytic degradation of Azo dye acid red 14 in water: investigation of the effect of operational parameters. J. Photochem. Photobiol. Chem. 157, 111–116. https://doi.org/10.1016/s1010-6030(03)00015-7.

Debanath, M.K., Karmakar, S., 2013. Study of blueshift of optical band gap in zinc oxide (ZnO-S) nanoparticles prepared by low-temperature wet chemical method. Mater. Lett. 111, 116–119. https://doi.org/10.1016/j.matlet.2013.08.069.

Devabharathi, V., Jagan, K.S.G., Priyan, S.R., Vidaarth, T.M.N., Surendhiran, S., Khadar, Y.A.S., Kandasamy, K., 2024. Rational design of NiO nanoflakes and porous GCN nanocomposite for synergic effectiveness on photocatalytic degradation of industry effluents and biological activity. Chem. Phys. Impact 8, 100637. https://doi.org/10.1016/j.chphi.2024.100637.

Doan Thi, T.U., Nguyen, T.T., Thi, Y.D., Ta Thi, K.H., Phan, B.T., Pham, K.N., 2020. Green synthesis of ZnO-S nanoparticles using orange fruit peel extract for antibacterial activities. RSC Adv. 10, 23899–23907. https://doi.org/10.1039/d0ra04926c.

Hadi, W.A., Shur, M.S., O'Leary, S.K., 2014. Steady-state and transient electron transport within the wide energy gap compound semiconductors gallium nitride and zinc oxide: an updated and critical review. J. Mater. Sci. Mater. Electron. 25, 4675–4713. https://doi.org/10.1007/s10854-014-2226-2.

Hanif, M., Munir, N., Abideen, Z., Yong, J.W.H., Elshikh, M.S., El-Keblawy, A., 2024. Synthesis and optimizations of nanoparticles from *Phragmites karka* improves tomato growth and salinity resilience. Biocatalyst and Agricultural Biotechnology 55, 102972. https://doi.org/10.1016/j.bcab.2023.102972.

Heibati, B., Yetilmezsoy, K., Zazouli, M.A., Rodriguez-Couto, S., Tyagi, I., Agarwal, S., Gupta, V.K., 2016. Adsorption of ethidium bromide (EtBr) from aqueous solutions by natural pumice and aluminium-coated pumice. J. Mol. Liq. 213, 41–47. https://doi.org/10.1016/j.molliq.2015.08.063.

Hitam, C.N.C., Jalil, A.A., 2020. A review on exploration of Fe_2O_3 photocatalyst towards degradation of dyes and organic contaminants. J. Environ. Manag. 258, 110050. https://doi.org/10.1016/j.jenvman.2019.110050.

Ishwarya, R., Vaseeharan, B., Kalyani, S., Banumathi, B., Govindarajan, M., Alharbi, N.S., Kadaikunnan, S., Al-Anbr, M.N., Khaled, J.M., Benelli, G., 2018. Facile green synthesis of zinc oxide nanoparticles using *Ulva lactuca* seaweed extract and evaluation of their photocatalytic, antibiofilm and insecticidal activity. J. Photochem. Photobiol., B 178, 249–258. https://doi.org/10.1016/j.jphotobiol.2017.11.006.

Jayappa, M.D., Ramaiah, C.K., Kumar, M.A.P., Suresh, D., Prabhu, A., Devasya, R.P., Sheikh, S., 2020. Green synthesis of zinc oxide nanoparticles from the leaf, stem and *in vitro* grown callus of *Mussaenda frondosa* L.: characterization and their applications. Appl. Nanosci. 10, 3057–3074. https://doi.org/10.1007/s13204-020-01382-2.

Jayasimha, H.N., Chandrappa, K.G., Sanaulla, P.F., Dileepkumar, V.G., 2024. Green synthesis of CuO nanoparticles: a promising material for photocatalysis and electrochemical sensor. Sens. Int. 5, 100254. https://doi.org/10.1016/j.sintl.2023.100254.

Jha, N., Madasamy, S., Prasad, P., Lakra, A.K., Esakkiraj, P., Tilwani, Y.M., Arul, V., 2023. Optimization and physicochemical characterization of polysaccharide purified from *Sonneratia caseolaris* mangrove leaves: a potential antioxidant and antibiofilm agent. Appl. Biochem. Biotechnol. 195, 7832–7858. https://doi.org/10.1007/s12010-023-04534-6.

Johnson, I.M., Kumar, S.G.B., Malathi, R., 2003. De-Intercalation of ethidium bromide and acridine orange by xanthine derivatives and their modulatory effect on anticancer agents: a study of DNA-directed toxicity enlightened by time correlated single photon counting. J. Biomol. Struct. Dyn. 20, 677–686. https://doi.org/10.1080/07391102.2003.10506884.

Kandasamy, K., Surendhiran, S., Jagan, K.S.G., Kumar, G.S., Khadar, Y.A.S., Rajasingh, P., 2023. Green synthesis of CdS quantum dots for photocatalytic and anti-corrosive applications in aqueous media. Appl. Surf. Sci. Adv. 13, 100364. https://doi.org/10.1016/j.apsadv.2022.100364.

Karthikeyan, S., Dhanakodi, K., Surendhiran, S., Jagan, K.S.G., Lenin, N., Dhatchinamurthy, L., Rajamanickam, A.T., 2023a. Sonochemical synthesis of Sn-Doped La2O3 nanoparticles and its application for the photocatalytic degradation of hazardous pollutants. J. Mater. Sci. Mater. Electron. 34. https://doi.org/10.1007/s10854-023-10561-0.

Karthikeyan, S., Dhanakodi, K., Surendhiran, S., Jagan, K.S.G., Thirunavukkarasu, P., Arunraja, L., 2023b. Effect of synthesis parameters on the structural, morphological characteristics, and photocatalytic activity of La2O3 nanoparticles. J. Indian Chem. Soc. 100, 100860. https://doi.org/10.1016/j.jics.2022.100860.

Kim, K.-M., Choi, M.-H., Lee, J.-K., Jeong, J., Kim, Y.-R., Kim, M.-K., Paek, S.-M., Oh, J.-M., 2014. Physicochemical properties of surface charge-modified ZnO-S nanoparticles with different particle sizes. Int. J. Nanomed. 9 (Suppl. 2), 41–56. https://doi.org/10.2147/IJN.S57923.

Kumar, S.G., Rao, K.S.R.K., 2015. Zinc oxide based photocatalysis: tailoring surface-bulk structure and related interfacial charge carrier dynamics for better environmental applications. RSC Adv. 5, 3306–3351. https://doi.org/10.1039/c4ra13299h.

Lavand, A.B., Malghe, Y.S., 2016. Visible-light photocatalytic degradation of ethidium bromide using carbon- and iron-modified TiO_2 photocatalyst. J. Therm. Anal. Calorim. 123, 1163–1172. https://doi.org/10.1007/s10973-015-5041-y.

Li, Z., Chang, P.-H., Jiang, W.-T., Liu, Y., 2020. Enhanced removal of ethidium bromide (EtBr) from aqueous solution using rectorite. J. Hazard. Mater. 384, 121254. https://doi.org/10.1016/j.jhazmat.2019.121254.

Liu, B., Wang, X., Wang, Y., Chen, X., Jin, X., Luo, X., 2023. Review of compounds and activities from mangrove *Sonneratia* genus and their endophytes. J. Holistic Integrative Pharm. 4, 218–227. https://doi.org/10.1016/j.jhip.2023.11.003.

Majumder, S., Chatterjee, S., Basnet, P., Mukherjee, J., 2020. ZnO-S based nanomaterials for photocatalytic degradation of aqueous pharmaceutical waste solutions – a contemporary review. Environ. Nanotechnol. Monit. Manag. 14, 100386. https://doi.org/10.1016/j.enmm.2020.100386.

Mandal, S., Pramanick, A., Chakraborty, S., Pratim Dey, P., 2020. Phase determination of ZrB_2-B_4C ceramic composite material using XRD and rietveld refinement analysis. Mater. Today 33, 5664–5666. https://doi.org/10.1016/j.matpr.2020.04.124.

Mohammed, G.H., Abdul Karim, H.J., 2021. Effect of some transitional metal oxides on the structural and optical properties of (ZnO-S-TiO_2) thin films. In: Proceedings of the PROCEEDINGS OF THE III INTERNATIONAL CONFERENCE ON ADVANCED TECHNOLOGIES IN MATERIALS SCIENCE, MECHANICAL AND AUTOMATION ENGINEERING: MIP: Engineering-Iii – 2021. AIP Publishing.

Nafisi, S., Saboury, A.A., Keramat, N., Neault, J.-F., Tajmir-Riahi, H.-A., 2007. Stability and structural features of DNA intercalation with ethidium bromide, acridine orange and methylene blue. J. Mol. Struct. 827, 35–43. https://doi.org/10.1016/j.molstruc.2006.05.004.

Nasiri, S., Rabiei, M., Palevicius, A., Janusas, G., Vilkauskas, A., Nutalapati, V., Monshi, A., 2023. Modified scherrer equation to calculate crystal size by XRD with high accuracy, examples Fe_2O_3, TiO_2 and V_2O_5. Nano Trends 3, 100015. https://doi.org/10.1016/j.nwnano.2023.100015.

Nath, M.R., Ahmed, A.N., Gafur, M.A., Miah, M.Y., 2018. Study on the Rietveld analysis for synthesized zinc oxide nanoparticles. AIP Conf. Proc. 1980, 030012. https://doi.org/10.1063/1.5044291.

Naum, Y., Pious, D.A., 1971. Reversible inhibition of cytochrome oxidase accumulation in human cells by ethidium bromide. Exp. Cell Res. 65, 355–359. https://doi.org/10.1016/0014-4827(71)90010-3.

Nguyen, L.T.T., Nguyen, T.T., Nguyen, H.N., Bui, Q.T.P., 2024. Analysis of active compounds and bioactivity of leaves extracts of *Sonneratia* species. Eng. Rep. 6. https://doi.org/10.1002/eng2.12870.

Ouchi, R.Y., Manzato, A.J., Ceron, C.R., Bonilla-Rodriguez, G.O., 2007. Evaluation of the effects of a single exposure to ethidium bromide in *Drosophila melanogaster* (Diptera-Drosophilidae). Bull. Environ. Contam. Toxicol. 78, 489–493. https://doi.org/10.1007/s00128-007-9208-5.

Pandimurugan, R., Thambidurai, S., 2016. Novel seaweed capped ZnO-S nanoparticles for effective dye photodegradation and antibacterial activity. Adv. Powder Technol. 27, 1062–1072. https://doi.org/10.1016/j.apt.2016.03.014.

Peiris, S., de Silva, H.B., Ranasinghe, K.N., Bandara, S.V., Perera, I.R., 2021. Recent development and future prospects of TiO₂ photocatalysis. J. Chin. Chem. Soc. 68, 738–769. https://doi.org/10.1002/jccs.202000465.

Pham, B.-T.T., Le, T.-K.T., Nguyen, T.T., Van Tran, T., Van Nguyen, D., Bui, Q.T.P., Phung, T.K., 2022. Polyvinyl alcohol based functional coating incorporated with *Sonneratia ovata* extract: preparation, characterization, and banana preservation. J. Appl. Polym. Sci. 139. https://doi.org/10.1002/app.52902.

Pham, B.-T.T., Nguyen, H.T.D., Nguyen, T.T., 2023. Release study of polyphenols from polyvinyl alcohol/chitosan active films supplemented with *Sonneratia ovata* extract and *Piper betel* (L.) essential oil. Food Packag. Shelf Life 40, 101174. https://doi.org/10.1016/j.fpsl.2023.101174.

Puspitasari, Y.E., Hardoko, H., Sulistiyati, T.D., Fajrin, A.N., Tampubolon, H.O., 2022. Identifikasi senyawa fitokimia dari daun mangrove *Sonneratia alba* dan analisis in silico sebagai antidiabetes. Jurnal Perikanan dan Kelautan 27, 241. https://doi.org/10.31258/jpk.27.2.241-248.

Raj, A., Lawerence, R., 2018. Green synthesis and characterization of ZnO-S nanoparticles from leafs extracts of *Rosa indica* and its antibacterial activity. Rasayan J. Chem. 11, 1339–1348. https://doi.org/10.31788/rjc.2018.1132009.

Ramesh, M., Anbuvannan, M., Viruthagiri, G., 2015. Green synthesis of ZnO-S nanoparticles using *Solanum nigrum* leaf extract and their antibacterial activity. Spectrochim. Acta Mol. Biomol. Spectrosc. 136, 864–870. https://doi.org/10.1016/j.saa.2014.09.105. Pt B.

Reema, R., Bedmutha, T., Kakati, N., Rayala, V.V.S.P.K., Radhakrishnanand, P., Juliya Devi, C., Thakur, D., Sankaranarayanan, K., 2024. Ethidium bromide degradation by cold atmospheric plasma in water and the assessment of byproduct toxicity for environmental protection. ACS Omega 9, 48044–48054. https://doi.org/10.1021/acsomega.4c04302.

Saber, O., Osama, A., Shaalan, N.M., Osama, M., 2024. Engineering the integration of titanium and nickel into zinc oxide nanocomposites through nanolayered structures and nanohybrids to design effective photocatalysts for purifying water from industrial pollutants. Catalysts 14, 340. https://doi.org/10.3390/catal14060340.

Saenger, P., Ragavan, P., Sheue, C.R., López-Portillo, J., Yong, J.W.H., Mageswaran, T., 2019. In: Gul, B., Böer, B., Khan, M., Clüsener-Godt, M., Hameed, A. (Eds.), Sabkha Ecosystems. Tasks for Vegetation Science, 49. Springer, pp. 379–400. https://doi.org/10.1007/978-3-030-04417-6_23.

Santika, F.T., Suyanto, H., Trisnawati, N.L.P., Indrayana, I.P.T., 2024. Determination of the optical band gap energy from the extraction and evaporation of anthocyanin compound sea lettuce (*Ulva lactuca* L.) using tauc plot method. BUL. FIS 25, 8. https://doi.org/10.24843/bf.2024.v25.i01.p02.

Saruchi, Verma, R., Kumar, V., Alothman, A.A., 2020. Comparison between removal of ethidium bromide and eosin by synthesized manganese (II) doped zinc (II) sulphide nanoparticles: kinetic, isotherms and thermodynamic studies. J. Environ. Health Sci. Eng. 18, 1175–1187. https://doi.org/10.1007/s40201-020-00536-2.

Shi, L.-E., Li, Z.-H., Zheng, W., Zhao, Y.-F., Jin, Y.-F., Tang, Z.-X., 2014. Synthesis, antibacterial activity, antibacterial mechanism and food applications of ZnO-S nanoparticles: a review. Food Addit. Contam. Part A Chem. Anal. Control Expo. Risk Assess 31, 173–186. https://doi.org/10.1080/19440049.2013.865147.

Silva, I.M.P., Byzynski, G., Ribeiro, C., Longo, E., 2016. Different dye degradation mechanisms for ZnO-S and ZnO-S doped with N (ZnO-S:N). J. Mol. Catal. Chem. 417, 89–100. https://doi.org/10.1016/j.molcata.2016.02.027.

Song, Y., Xu, L., Wu, Q., Xiao, S., Zeng, H., Gong, Y., Li, C., Cheng, S., Li, Q., Zhang, L., et al., 2020. A new strategy to reduce toxicity of ethidium bromide by alternating anions: new derivatives with excellent optical performances, convenient synthesis, and low toxicity. Small Methods 4, 1900779. https://doi.org/10.1002/smtd.201900779.

Subramani, K., Ganeshan, J.K.S., Srinivasan, S., Mohanasundaram, N.V.T., Incharoensakdi, A., 2025. Hydrothermally and green synthesized TiO₂ nanoparticles with high photocatalytic textile industry dye degradation, antibacterial and antioxidant activities. J. Alloys Compd. 1017, 179068. https://doi.org/10.1016/j.jallcom.2025.179068.

Subramanian, H., Krishnan, M., Mahalingam, A., 2021. Photocatalytic dye degradation and photoexcited anti-microbial activities of green zinc oxide nanoparticles synthesized via *Sargassum muticum* extracts. RSC Adv. 12, 985–997. https://doi.org/10.1039/d1ra08196a.

Sun, C., Yang, J., Xu, M., Cui, Y., Ren, W., Zhang, J., Zhao, H., Liang, B., 2022. Recent intensification strategies of SnO₂-based photocatalysts: a review. Chem. Eng. J. 427, 131564. https://doi.org/10.1016/j.cej.2021.131564.

Swetha, S., Balakrishna, R.G., 2011. Preparation and characterization of high activity zirconium-doped anatase Titania for solar photocatalytic degradation of ethidium bromide. Chinese J. Catalysis 32, 789–794. https://doi.org/10.1016/s1872-2067(10)60200-8.

Tan, Y.Y., Wong, L.S., Nyam, K.L., Wittayanarakul, K., Zawawi, N.A., Rajendran, K., Djearamane, S., Dhanapal, A.C.T.A., 2023. Development and evaluation of topical zinc oxide nanogels formulation using *Dendrobium anosmum* and its effect on *Acne vulgaris*. Molecules 28, 6749. https://doi.org/10.3390/molecules28196749.

Torkamani, R., Aslibeiki, B., Fathi, S., 2023. Competition between the effect of particle size and TM-Doping on photodegradation of oxytetracycline using Zn0.94M0.06O (M: Mn, Fe, Co, Ni, Cu and Zn) nanoparticles. React. Kinet. Mech. Catal. 136, 2737–2749. https://doi.org/10.1007/s11144-023-02477-x.

Tsuboi, M., Benevides, J.M., Thomas Jr., G.J., 2007. The complex of ethidium bromide with genomic DNA: structure analysis by polarized raman spectroscopy. Biophys. J. 92, 928–934. https://doi.org/10.1529/biophysj.106.093633.

Vacquier, V.D., Brachet, J., 1969. Chromosomal abnormalities resulting from ethidium bromide treatment. Nature 222, 193–195. https://doi.org/10.1038/222193a0.

Wang, R., Tan, H., Zhao, Z., Zhang, G., Song, L., Dong, W., Sun, Z., 2014. Stable ZnO-S@TiO2 core/shell nanorod arrays with exposed high energy facets for self-cleaning coatings with anti-reflective properties. J. Mater. Chem. A Mater. Energy Sustain. 2, 7313–7318. https://doi.org/10.1039/c4ta00455h.

von Wurmb-Schwark, N., Cavelier, L., Cortopassi, G.A., 2006. A low dose of ethidium bromide leads to an increase of total mitochondrial DNA while higher concentrations induce the MtDNA 4997 deletion in a human neuronal cell line. Mutat. Res. 596, 57–63. https://doi.org/10.1016/j.mrfmmm.2005.12.003.

Xie, E., Zheng, L., Ding, A., Zhang, D., 2021. Mechanisms and pathways of ethidium bromide fenton-like degradation by reusable magnetic nanocatalysts. Chemosphere 262, 127852. https://doi.org/10.1016/j.chemosphere.2020.127852.

Ye, Y., Feng, Y., Bruning, H., Yntema, D., Rijnaarts, H.H.M., 2018. Photocatalytic degradation of metoprolol by TiO₂ nanotube arrays and UV-LED: effects of catalyst properties, operational parameters, commonly present water constituents, and photo-induced reactive species. Appl. Catal., B 220, 171–181. https://doi.org/10.1016/j.apcatb.2017.08.040.

Yin, I.X., Zhang, J., Zhao, I.S., Mei, M.L., Li, Q., Chu, C.H., 2020. The antibacterial mechanism of silver nanoparticles and its application in dentistry. Int. J. Nanomed. 15, 2555–2562. https://doi.org/10.2147/IJN.S246764.

Zandi, M., Kameli, P., Salamati, H., Ahmadvand, H., Hakimi, M., 2011. Microstructure and optical properties of ZnO-S nanoparticles prepared by a simple method. Phys. B Condens. Matter 406, 3215–3218. https://doi.org/10.1016/j.physb.2011.05.026.

Zhang, D., Lv, S., Luo, Z., 2020. A study on the photocatalytic degradation performance of a [KNbO3]0.9-[BaNi0.5Nb0.5O3-δ]0.1 perovskite. RSC Adv. 10, 1275–1280. https://doi.org/10.1039/c9ra07310h.

Zimmer, M., Ajonina, G.N., Amir, A.A., Cragg, S.M., Crooks, S., Dahdouh-Guebas, F., Duke, N.C., Fratini, S., Friess, D.A., Helfer, V., Huxham, M., Kathiresan, K., Kodikara, K.A.S., Koedam, N., Lee, S.Y., Mangora, M.M., Primavera, J., Satyanarayana, B., Yong, J.W.H., Wodehouse, D., 2022. When nature needs a helping hand: Different levels of human intervention for mangrove (re-)establishment. FRONTIERS IN FORESTS & GLOBAL CHANGE 5, e784322. https://doi.org/10.3389/ffgc.2022.784322.